Position-based Dynamics Simulator of Vessel Deformations for Path Planning in Robotic Endovascular Catheterization

Zhen Li[a,b,*], Enrico Manzionna[a], Giovanni Monizzi[c], Angelo Mastrangelo[c], Maria Elisabetta Mancini[c], Daniele Andreini[c,d], Jenny Dankelman[b], Elena De Momi[a]

[a]*Department of Electronics, Information and Bioengineering, Politecnico di Milano, Piazza Leonardo da Vinci 32, 20133 Milan, Italy*
[b]*Department of Biomechanical Engineering, Delft University of Technology, Mekelweg 2, 2628 CD Delft, Netherlands*
[c]*Centro Cardiologico Monzino, IRCCS, Milan, Italy*
[d]*Department of Clinical Sciences and Community Health, University of Milan, Milan, Italy*

Abstract

A major challenge during autonomous navigation in endovascular interventions is the complexity of operating in a deformable but constrained workspace with an instrument. Simulation of deformations for it can provide a cost-effective training platform for path planning. Aim of this study is to develop a realistic, auto-adaptive, and visually plausible simulator to predict vessels' global deformation induced by the robotic catheter's contact and cyclic heartbeat motion. Based on a Position-based Dynamics (PBD) approach for vessel modeling, Particle Swarm Optimization (PSO) algorithm is employed for an auto-adaptive calibration of PBD deformation parameters and of the vessels movement due to a heartbeat. *In-vitro* experiments were conducted and compared with *in-silico* results. The end-user evaluation results were reported through quantitative performance metrics and a 5-Point Likert Scale questionnaire. Compared with literature, this simulator has an error of 0.23±0.13% for deformation and 0.30±0.85mm for the aortic root displacement. *In-vitro* experiments show an error of 1.35±1.38mm for deformation prediction. The end-user evaluation results show that novices are more accustomed to using joystick controllers, and cardiologists are more satisfied with the visual authenticity. The real-time and accurate performance of the simulator make this framework suitable for creating a dynamic environment for autonomous navigation of robotic catheters.

Keywords: Simulation, Optimization, Steerable Catheter, Deformable Environment, Intervention, Medical Robotics

1. Introduction

Vascular disease is a common, abnormal condition of blood vessels, and it can be severe. Narrowed or obstructed arteries, typically due to atherosclerosis, affect blood circulation. Percutaneous Coronary Intervention (PCI) is a reliable and valid procedure for patients with symptomatic coronary stenosis. Based on patient characteristics, different access sites can be selected. Among them, radial access is recommended (Class I, Level A) as the standard approach due to its fewer vascular complications compared with the transfemoral approach [1].

Intra-operative path planning and control for a robotic catheter will increase the level of autonomy in medical robotics [2]. Vessel deformations in these procedures can be very high. The displacement of vessels due to the collision of the catheter with the aortic wall were quantified in [3, 4, 5]: the aortic bifurcation was mostly displaced in a cranial direction with the median craniocaudal dislocation of 6.7 mm (min 2.1 mm, max 12.3 mm). A displacement at the aortic bifurcation of 1.4 ± 1.1 mm was reported due to the passing of a stiff guidewire [6]. This deformation of vessels makes robotic catheterization very challenging and will require training. For training, a virtual endovascular catheterization system that simulates the characteristics of percutaneous devices and the vasculature can provide cost-effective and safe training environment for robotic catheter manipulation compared with phantoms, *ex-vivo* or *in-vivo* experiments. Moreover, important intra-operative data can be collected (e.g., the catheter tip trajectory) and post-processed to gain valuable insight for improving the outcome and developing autonomous interventions [7]. Peral-Boiza *et al.* [8] presented a virtual reality training platform involving the progress of a flexible endoscope with a steerable tip into a virtual rigid vascular phantom. Hao *et al.* [9] proposed a personalized cardiovascular intervention simulation system that can simulate the complex interactions between vessels and tipped guidewires.

To model and simulate intra-operative vessel deformations, different prediction approaches were developed using Mass Spring Model (MSM) [10], Finite Element Method (FEM) [6], and Position-based Dynamics (PBD) [11]. Compared with the first two methods, PBD is more suitable for real-time simulations because it does not need a complex mesh generation [11, 12, 13]. Although PBD is not as accurate as other methods, its high efficiency and close match to real deformations have been reported [14, 15]. However, PBD parameters do not have physical meanings, and thus they should be properly tuned.

Different modeling methods for catheters and guidewires are

*Corresponding author
Email address: zhen.li@polimi.it; z.li-13@tudelft.nl (Zhen Li)

studied. PBD and shape matching approaches were applied for endoscope modeling [8]. FEM, MSM [16], and rigid multibody links [17] were also developed for catheters and guidewires [18]. Concerning the steerable tip, Cosserat rod [19], elastic rod [9], constant-curvature [20], and rigid-link [21] were extensively exploited as modeling approaches of steerable devices. While the Cosserat rod provides an exact solution to the static equilibrium of the device, the computational complexity and cost become high when extending the modeling to dynamics. On the other hand, the rigid-link modeling approach is well-established, but the number of variables increases dramatically when a realistic model is of interest. Constant curvature modeling may constitute a valuable trade-off between Cosserat rod's complications and assumptions of rigid-link models [22].

Although state-of-the-art research investigates deformations of vessels due to the device's contact, vessels movement due to heartbeat motion, and the robotic catheter's steerability, a modeling and simulation method involving all those components in one individual framework has not been reported yet. Compared to literature, there are three significant contributions in this work: (1) The deformations of vessels due to the device's contact are globally distributed, instead of a local deformation by activating an individual bounding box as in Ye *et al.*'s work [11]; (2) It involves the vessels movement due to heartbeat motion; (3) It uses a more general and autonomous approach for patient-specific parameters calibration.

2. Materials and Methods

2.1. Modeling Method of Vasculature

Mimicking intra-operative deformations is essential for providing a dynamic environment in robotic system simulation. To achieve this goal, we propose a vasculature deformation framework depicted in Fig. 1 (top left) that illustrates the workflow of a patient-specific vessel mesh model extracted from Computed Tomography Angiography (CTA) images and deformed via the PBD approach. A series of optimization processes were performed to calibrate our modeling and simulation framework. To simulate the deformable properties of the aorta accurately, the vasculature PBD parameters were calibrated using Particle Swarm Optimization (PSO) based on the data reported in the reference [11]. Vessels movement due to a heartbeat was also calibrated through PSO according to the cyclic movement of the aortic annulus [23].

The data collection followed the ethical protocol approved by the Centro Cardiologico Monzino (CCM) under the assigned code of *02_21 PA*. The CTA images are from a patient with cardiac disease. The simulation environment was developed in *Unity* 2020.3.7 using *NVIDIA FleX* on a workstation equipped with an Intel Core i9-9900KF CPU @3.60GHz processor, 32GB RAM, NVIDIA GeForce GTX 1660 GPU with CUDA 11.0. The time step of the simulation was set as 0.02 s.

2.1.1. Vasculature reconstruction

First, we extracted a vessel mesh model from CTA images. Pre-operative CTA images were acquired following the typical Multidetector Computed Tomography (MDCT) scan strategies: cardiac Electrocardiogram (ECG)-synchronized CTA of the aortic root and heart followed by a non-ECG-synchronized helical CTA of the thorax, abdomen and pelvis. Respiratory motion is also a common artifact seen in cardiac CT [24]. There are novel studies regarding motion correction under a free-breathing acquisition mode [25, 26]. In this study, a breath-holding method was employed for CT scan acquisition, and the respiratory motion was assumed to be negligible. The image data were acquired with a voxel size of 0.789×0.789×0.625 mm and a voxel number of $512 \times 512 \times 832$.

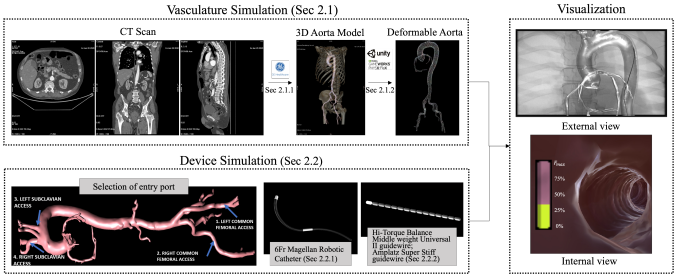

Figure 1: Overview of the proposed modeling and simulation system, presenting the workflow from the extraction of the patient-specific deformable vessel mesh model (top left, Sec 2.1) and the device simulation procedure (bottom left, Sec 2.2) to the visualization of the simulated training environment (right).

Semi-automatic segmentation of the vessels and 3D mesh model reconstruction were performed using the *AW server* (GE Healthcare), followed by a manual refinement process. The 3D models with embedded lesions were exported under the support of the *3D suite* (GE Healthcare). After that, to better represent the aortic geometry and avoid undesired section distortion, a constant thickness of 1 mm was constructed for the aorta and a thickness of 0.55 mm for the coronaries using *Meshmixer* (Autodesk, Inc., CA, US), considering that the thickness of aorta is between 0.97 mm and 1.99 mm [27] and the thickness of coronaries is between 0.55 mm and 1 mm [28]. Post-processing was applied using *MeshLab* (ISTI - CNR) [29] by applying a simplification of the mesh with the quadratic edge collapse decimation with a default quality threshold of 0.3 and the target number of faces of 7000. Finally smoothing was carried out using a Taubin smoothing technique [30] with scaling factors $\lambda = 0.5$, $\mu = -0.53$ and 10 smoothing steps.

2.1.2. Position-based dynamics (PBD) approach

As first proposed by Müller *et al.* [31], the PBD approach discretizes an object into a particle system composed of a set of particles. Then it computes the time evolution of the system by directly updating particles positions, subject to a set of equality and inequality constraints. The type of constraints among particles can influence the system's behavior. For generating deformations of objects, a multi-cluster shape matching constraint [32] is considered. Specifically, the particle system is represented as a set of clusters, and the clusters can overlap. Since one particle can belong to multiple clusters, the final position correction is obtained by averaging all goal positions of the belonging clusters.

Table 1: PBD parameters kept constant for all simulations.

Category	Parameter	Value
FleX Container	Particle Radius	3.0 mm
	Solid Rest	2.5 mm
	Particle Friction	0.1
	Collision Distance	2.5 mm
FleX Soft Asset	Particle Spacing	2.1 mm
	Surface Sampling	6.0
FleX Soft Skinning	Skinning Falloff	100
	Skinning Max Distance	20

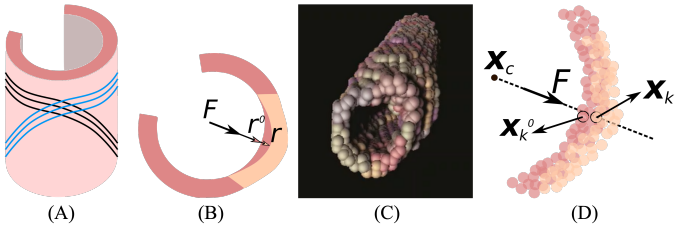

Figure 2: Overview of the steps to obtain the strain: (A) Based on the simplified geometry of fibers, (B) we apply an external force ($\boldsymbol{F}$) in the radial direction (B) on the vasculature particle system. (D) Then the change of radius (r^0, r) is converted from the particle position ($\boldsymbol{x}_k^0, \boldsymbol{x}_k$).

The PBD approach implementation is based on the simulation library *NVIDIA FleX*. A realistic elastic behavior is obtained by appropriately selecting cluster-related parameters: cluster spacing (s_c, the distance between adjacent clusters), cluster radius (r_c, the radius of each cluster region) and cluster stiffness ($t_c \in [0, 1]$, the extent to which adjacent cluster are constrained to each other). The cluster spacing and radius would influence the overlapping of adjacent clusters and the particles' goal positions.

The other PBD parameters keep their values fixed across all the simulations (See Table 1). The particle spacing and particle radius are set in accordance with the following rules: the number of particles that discretizes the whole aorta should be less than 10000, which is the maximum allowable number in *NVIDIA FleX*, and the particle spacing should be less than the two times of particle radius to maintain connectivity. The solid rest and collision distance were set to 2.5 mm respecting the particle radius. Furthermore, the flex soft skinning was determined for proper mesh rendering. As boundary conditions for the simulation, we applied a fixed constraint, that removes all degrees of freedom of movement, to the particles of selected regions, such as the distal extremities of the internal and external iliac arteries, of supraaortic vessels and of coronaries.

2.1.3. Vasculature PBD calibration

In this study, the stress-strain curve from [11] is used for calibration. Ye *et al.* [11] presented a geometric vessels model and recorded a sequence of the forces acting on the vertex in the inner wall and the subsequent displacement. A stress-strain curve ($\sigma - \epsilon$) was obtained, which depicts the biomechanics properties appropriately as reported [11]. In order to obtain the stress-strain curve from the virtual system, we made an assumption for simplicity.

Assumption 1: We assume the vessels can be considered as a composition of two main families of fibers, which are axially symmetric to each other (Fig. 2A). Two fibers yield the same contribution along the circumferential direction.

Therefore, the whole fiber's stretching is directly linked to the extension in the circumferential direction. The displacements along the circumference can be associated with the elongation or shortening of the vessels' internal radius (Fig. 2B). We apply an external force ($\boldsymbol{F}$) on the vasculature in the radial direction and compute the change of radius (initial radius r^0, deformed radius r) from the particle position. Specifically, we apply an external distributed force ($\boldsymbol{F}$) on the vasculature particle system over a surface with an area of A in the radial direction (Fig. 2C). At a specific mark (i.e., the k-th particle), its position is deformed from $\boldsymbol{x}_k^0$ to $\boldsymbol{x}_k$ in a three-dimensional space (Fig. 2D). Thus we estimate the internal radius by computing the distance from the particle to the center of the cross-section of vessels $\boldsymbol{x}_C$:

$$r^0 = \|\boldsymbol{x}_k^0 - \boldsymbol{x}_C\| \tag{1}$$

$$r = \|\boldsymbol{x}_k - \boldsymbol{x}_C\| \tag{2}$$

Therefore, the stress-strain curve is computed by:

$$\sigma = \|\boldsymbol{F}\|/A \tag{3}$$

$$\epsilon = (r - r^0)/r^0 \tag{4}$$

The Particle Swarm Optimization (PSO) approach [33] is employed to optimize the PBD cluster parameters (s_c, r_c, t_c) by minimizing the Root Mean Square Error (RMSE) (e_v) compared with the reference stress-strain curve:

$$\min_{s_c, r_c, t_c} e_v \quad \text{with } e_v = \sqrt{\frac{\sum_{m=1}^{M} (\hat{\epsilon}_m - \epsilon_m)^2}{M}} \tag{5}$$

where $\hat{\epsilon}_m$ is the mth strain of the reference stress-strain curve and ϵ_m is the mth strain of the simulated strain stress curve with m that spans from 0 to M, where M is the total number of samples.

The PSO algorithm considers each solution as a particle of a swarm that moves through the search space to find an optimal position. Each particle has a position $\boldsymbol{\chi}_i = (x_i^1, x_i^2, ..., x_i^N)$ and a velocity $\boldsymbol{v}_i = (v_i^1, v_i^2, ..., v_i^N)$ in a N-dimensional configuration space, where i denotes the ith particle and N represents the dimension of the configuration or number of unknown variables. During every iteration, each particle is updated by following two "best" values: the position vector of the local optimal solution ("cognitive" item) this particle has achieved so far and the global optimal position ("social" item), obtained so far, by any particle in the population according to:

$$\begin{aligned} \boldsymbol{v}_i^k &= w\boldsymbol{v}_i^k + c_1 u_1 ({}^*p_i^k - \boldsymbol{\chi}_i^k) + c_2 u_2 ({}^*g^k - \boldsymbol{\chi}_i^k) \\ \boldsymbol{\chi}_i^{k+1} &= \boldsymbol{\chi}_i^k + \boldsymbol{v}_i^{k+1} \end{aligned} \tag{6}$$

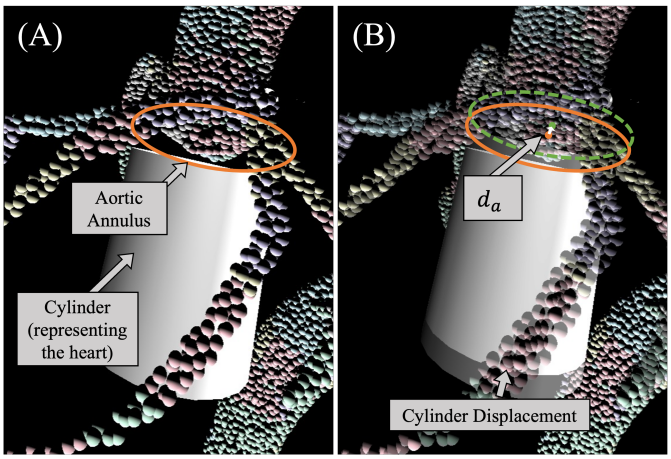

Figure 3: Simulation scheme for heartbeat movement: a colliding cylinder representing the heart applies an external force on the aortic root , and causes annulus displacement d_a between two subsequent time steps (A) and (B).

where $\boldsymbol{v}_i^k$ is the velocity of the ith particle at the kth iteration, and $\boldsymbol{\chi}_i^k$ is the current position of the ith particle at the kth iteration. c_1, c_2 are positive constants, and u_1, u_2 are two random variables with an uniform distribution between 0 and 1. In this equation, w is the inertia weight which shows the effect of the previous velocity vector on the new vector, ${}^*p$ is the local optimal and ${}^*g$ is the global one. The hyperparameters of the PSO algorithm were set as $c_1 = 0.5$, $c_2 = 0.3$ and $w = 0.3$.

The reference curve with a range of $[0, 0.58]$ MPa [11] was sampled with a constant interval of 0.02 MPa stress. Those values were given as an external force to the aortic wall using Eq. 3 and the corresponding strains were computed with Eq. 4. Once the stress-strain curve was obtained, its RMSE e_v was computed relative to the reference and regarded as the particle penalty. At this point, the PSO algorithm tries to reduce the penalty by updating the particles of the swarm (i.e., cluster parameters in this case) in the following iteration. Since PSO does not use the gradient of the objective function, it does not need to be differentiable. Moreover, PSO can evolve into more complicated and customized problems.

2.1.4. Heartbeat movement and calibration

To mimic the vessel movement due to a heartbeat, we applied a time-varying external force $f(t)$ on the aortic root through a colliding cylinder representing the heart (See Fig. 3). Using the optimal PBD parameters obtained from the vasculature calibration, the heartbeat calibration process looks for the optimal external forces that generate the heartbeat movement. The displacement of the cylinder was tuned with respect to the referred cyclic movement of the aortic annulus [23].

The annulus displacement d_a is defined as the longitudinal displacement of the particles on the aortic annulus.

$$d_a(t) = z_a(t) - z_a^0 \tag{7}$$

where $z_a(t)$ is the average longitudinal position of the particles sampling the aortic annulus at the current time and z_a^0 is that position in the rest state (i.e., at the initial time). The PSO approach is employed to optimize these values by minimizing the RMSE e_a between the simulated and real aortic annulus displacement d_a with respect to the time t.

$$\min_{f(0)\cdots f(T_f)} e_a \quad \text{with } e_a = \sqrt{\frac{\sum_{t=0}^{T_f}(\hat{d}_a(t) - d_a(t))^2}{T_f}} \tag{8}$$

where $\hat{d}_a(t)$ is the annulus displacement of the reference curve at time t and $d_a(t)$ is the simulated annulus displacement at time t with t that spans from 0 to T_f, where T_f is the total number of samples for heartbeat calibration.

2.1.5. Force bar visualization

To provide visual feedback of the collision force when the device tip collides with the vessel wall, we obtained an absolute collision force along the entire device shaft via Newton's Second Law of Motion and computed a ratio between the force and the maximum force [34]. The maximum force denotes the most insecure value that the user could apply. For example, the maximum force is set as 0.8 N in femoral arteries, 0.8 N in the aorta, 0.6 N in coronaries, and 0.8 N in subclavian arteries [34].

Only when the device tip collides with the vessel wall, the contact force is considered, and the contact force is considered along the entire device shaft. We made this assumption because end-user interviews revealed that the cardiologists focus more on the device tip for safety reasons. A mean filtering method is applied to force computation. Therefore the force is sometimes non-zero in the force bar visualization when the tip does not seem to be in contact.

2.2. Modeling Method of Devices

2.2.1. Steerable catheter

Steerable catheters have one or even more bendable segments to help navigate into the coronary ostium. Each steerable segment has three controllable movements: bending, rotating and advancing. Constant curvature modeling may constitute a valuable trade-off between the Cosserat rod's complications and the assumptions of rigid-link models [22].

The constant-curvature modeling method considers a continuum device as a set of finite curved links. These links are represented by a set of arc parameters, converted into analytical frame transformations. For each steerable segment, we assume that its shape is an arc with constant curvature κ at different bending angles, arc center at C, and a total length of l. Figure 4A illustrates the segment base frame $\mathcal{F}_b$ convention chosen, considering z-axis tangent to the base of the segment. The configuration space is defined by arc parameters: the rotation angle around z-axis $\phi \in [0, 2\pi]$, the arc length $s \in [0, l]$, and the arc curvature κ which entails the segment bending angle $\beta = \kappa s$.

Given the configuration space (κ, ϕ, s), we perform the transformation ${}^b\boldsymbol{T}_i$ from the segment base frame $\mathcal{F}_b$ to frame $\mathcal{F}_i$ at any point ($\boldsymbol{p}_i = [x, y, z]^T, i \in [0, G]$) along the arc, according to the employed D-H table parameterization approach [35]. Then the position $\boldsymbol{p}_i$ in the global frame $\mathcal{F}_0$ can be expressed as:

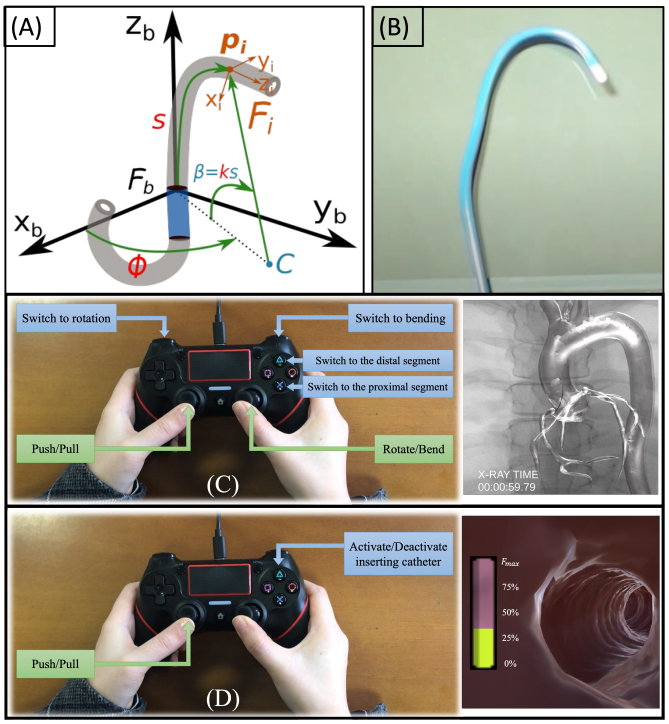

Figure 4: (A) Parameterization of the steerable segment modeling: ϕ denotes the arc rotation angle around z-axis, s is the arc length at $\boldsymbol{p}_i$, and κ is the arc curvature. C denotes the arc center. (B) Megellan robotic catheter. The joystick controller settings for (C) steerable catheter and (D) flexible guidewire. The GUI includes a fluoroscopy view with operation time, and an internal view with visual feedback of collision force.

$$[\boldsymbol{p}_i^T \quad 1]^T = \boldsymbol{T}_b \cdot {}^b\boldsymbol{T}_i \cdot {}^i\boldsymbol{p}_i \text{ with } {}^i\boldsymbol{p}_i = [0,0,0,1]^T \tag{9}$$

where $\boldsymbol{T}_b$ denotes the transformation matrix from the global frame $\mathcal{F}_0$ to the segment based reference frame $\mathcal{F}_b$, and ${}^i\boldsymbol{p}_i$ denotes the origin of $\mathcal{F}_i$ (i.e., $\boldsymbol{p}_i$) expressed in $\mathcal{F}_i$.

This transformation allows the mapping from the arc parameters space to the task space ($\boldsymbol{p}_i$). By emerging all steerable segments connected with a rigid link, the robotic catheter can reach multiple points in 3-D space and realize the typical catheterization movements performed in a clinical environment, namely, push/pull, bend, and rotate.

As a proof of concept, we built the 6Fr Magellan Robotic Catheter (Hansen Medical, USA) model (Fig. 4B) with the following specification: distal bending segment length of 30 mm, proximal bending segment length of 25 mm, guide articulation angle of 140° for distal bend and 60° for the proximal bend.

2.2.2. *Flexible guidewire*

A flexible guidewire advances through vessels to reach the target position and provides a rough reference path for catheters. The flexible guidewire modeling employs the MSM-based method [16]. For the modeling implementation in *Unity*, the guidewire consists of a set of capsules linked together with a configurable joint component that are linear springs along the longitudinal direction of the guidewire with a certain stiffness K_s.

We provided two flexible guidewire models as a user choice. We built the softer coronary guidewire model referring to the Hi-Torque Balance Middleweight Universal II guidewire (Abbot, Illinois, USA) [17] with the following specifications: an internal diameter D_{int} of 0.014 inches (0.356mm), and a bending stiffness K_b of 75 Nmm^2. We built the stiffer femoral guidewire model referring to the Amplatz Super Stiff (Boston Scientific, Massachusetts, USA) [36] with the following specifications: an internal diameter D_{int} of 0.035 inches (0.889mm), and a bending stiffness K_b of 1850 Nmm^2.

Therefore, the moment of inertia I is derived as

$$I = \pi D_{int}^4/64 \tag{10}$$

and the Young Modulus E is expressed as

$$E = K_b/I \tag{11}$$

To the end, the stiffness K_s can be then computed as

$$K_s = EA_s/L \tag{12}$$

where K_s is the stiffness of the spring, E is the Young Modulus (which is 8.5 GPa for Hi-Torque, and 60 GPa for Amplatz), A_s is the cross section of the spring and L is the distance between the joints.

In order to mimic the follow-the-wire movement of the catheter-guidewire pair and provide a more realistic visual authenticity, during the advancement of the guidewire, a flexible catheter with a bigger diameter and with referenced mechanical properties as in [37] can be inserted following the guidewire. The combined system (i.e., catheter over a guidewire) is more rigid since the stiffness of the spring is computed as a combination of those two objects:

$$\begin{aligned} K &= K_{gu} + K_{ca} \\ K_{ca} &= \pi E_{ca}(D_{ec}^2 - D_{ic}^2)/4 \end{aligned} \tag{13}$$

where K, K_{gu}, K_{ca} is the stiffness of the resulting system, the guidewire, and the reference catheter. E_{ca} is the Young modulus of the reference catheter, D_{ec}, D_{ic} is the external and internal diameter of the reference catheter. Moreover, the mechanical property of the catheter [37] is specified as E_{ca} of 85.5 GPa, D_{ec} of 2.96 mm, and D_{ic} of 2.51 mm.

2.2.3. *Guiding controller for devices*

The guiding system of devices is a CHEREEKI controller (Fig. 4C-D) by which the user can move the guidewire and the robotic catheter in a push-pull configuration, and bend-rotate at the distal/proximal segments of the robotic catheter. The Graphical User Interface (GUI) provides a fluoroscopy view, an internal view, visual feedback of collision force, and operation time (Fig. 4). The users can select starting sites and devices according to their preference.

2.3. *In-vitro Setup*

In-vitro experiments were conducted for the deformed model validation. We compared the displacement obtained during

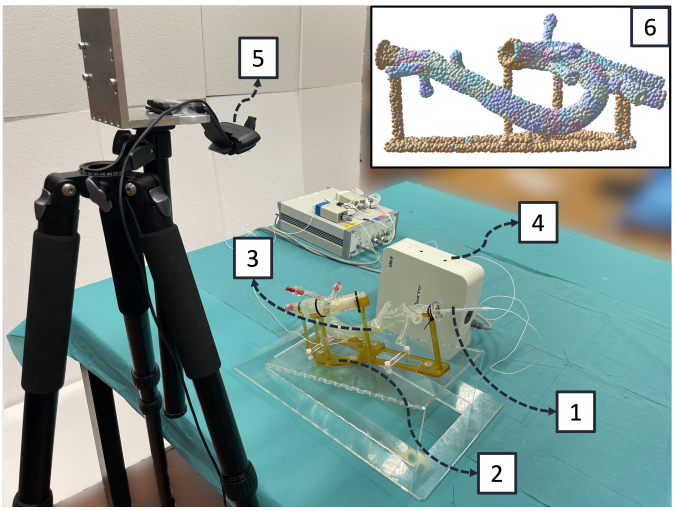

Figure 5: The *in-vitro* experimental setup: 1) a catheter with EM sensor embedded at the tip 2) an aortic phantom with support 3) the second EM sensor attached to the surface of the phantom 4) Aurora EM field generator 5) an external camera for filming the experiments 6) The PBD model in the simulator with fixed particles marked in orange.

catheter contacts simulated on our PBD model (*in-silico*) and the ones obtained on the aortic phantom (*in-vitro*).

The *in-vitro* experimental setup is presented in Fig. 5. Experiments were performed in a transparent, deformable silicone aortic phantom (Materialise NV, Leuven, Belgium) [38, 39]. This phantom is a dedicated synthethic test bed developed by the EU-funded project CASCADE. The silicon model fabrication includes segmentation of CT data, 3D printing of patient specific shells and vacuum casting of the silicon model. The realistic mechanical properties of the deformable phantom were verified through uniaxial tensile tests. See [38, 39] for more details. The phantom was placed on a 3D printed support designed to preserve the anatomical vascular orientation. We used a polyethylene tube, with an outer diameter of 5 mm and stiffness of 0.245 GPa [40], as a catheter to push it against the aortic wall to validate phantom deformation alone. An Electromagnetic (EM) sensor (Northern Digital Inc., Waterloo, Canada) was embedded at the tip of the catheter to track its position. The setup also includes the second EM sensor attached to the surface of the phantom, Aurora EM field generator, and an external camera for filming the experiments. The PBD model in the simulator with fixed particles marked in orange is also shown in Fig. 5.

The vessel deformation obtained *in-vitro* is defined as the displacement d_{em} of the EM sensor attached to the surface of the phantom. It indicates the ground-truth deformation.

$$d_{em} = \|\boldsymbol{x}_{em} - \boldsymbol{x}_{em}^0\| \tag{14}$$

where $\boldsymbol{x}_{em}^0$ is the initial position of the EM sensor attached to the surface of the phantom, and $\boldsymbol{x}_{em}$ is the current position.

The vessel deformation obtained *in-silico* is presented as the displacement d_k of the particle corresponding to the EM sensor position in the PBD model. It indicates the simulated deformation.

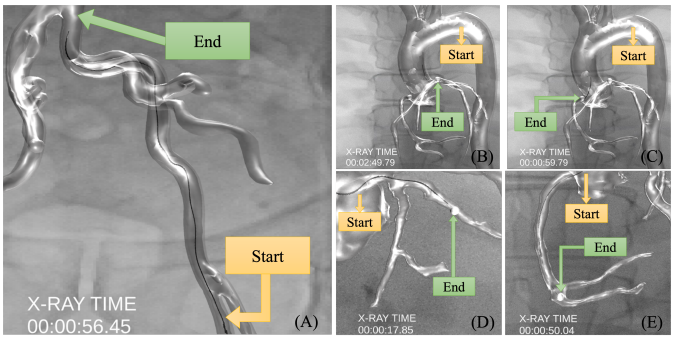

Figure 6: The operation tasks: (A) To advance the guidewire from femoral arteries to the abdominal aorta; (B) To advance the robotic catheter from the aortic arch to the left coronary ostium or (C) the right one; (D, E) To advance the guidewire from the coronaries ostium to the target position in the coronaries. A simulated demo of intervention tasks is made available: https://youtu.be/jdfQeZnBLhs

$$d_k = \|\boldsymbol{x}_k - \boldsymbol{x}_k^0\| \tag{15}$$

where the particle position is deformed from $\boldsymbol{x}_k^0$ to $\boldsymbol{x}_k$ in a three-dimensional space.

2.4. End-user Validation Protocol

The validity and visual authenticity of the virtual system were evaluated by cardiologists from CCM, IRCCS, Milan, Italy. The users are composed of ten experts (medical doctors from CCM, experience level 6.4±4.9 years, including two coauthors GM and AM) and ten novices (six medical doctors from CCM, experience level < 1 year, and four bioengineers). The users were asked to test the usability of the simulator by performing specific operation tasks of PCI (Fig. 6).

For each operation task, their performance matrices are recorded. For evaluating user skills playing with the simulator, two parameters are proposed as performance matrices: playtime (if larger, it means a longer time of exposure to X-rays and a higher risk of infection for the patient), accumulated collision during the whole path (if larger, it means a higher risk of vascular rupture due to contact with the device).

The users did not have any previous training on the simulator and they had two chances to perform the task: the first one to learn how to use the simulator and the second one to record their scores.

Afterwards, the users were asked to fill a questionnaire to help improve the simulator development. The questionnaire stated 11 questions, and for each question, the users can insert their level of agreement, according to the 5-Point Likert Scale.

3. Results

3.1. Calibration Results

3.1.1. Vasculature PBD calibration

To obtain the optimal cluster parameters, we applied an external stress perpendicular to the vessel wall with the range of $[0, 0.58]$MPa and measured the displacement of the particles

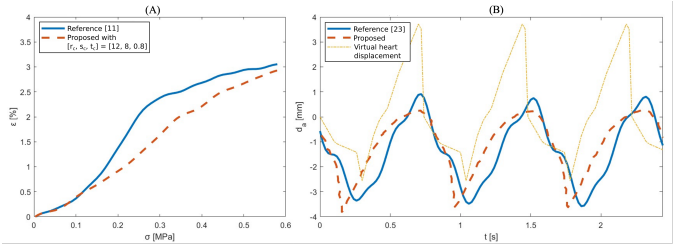

Figure 7: Quantitative comparison results between simulator performance and literature: (A) The vessels stress-strain curve ($\sigma - \epsilon$) from literature (blue) and from the optimal case after calibration using PSO algorithm (red). (B) The annulus displacement (d_a) along time t from literature (blue) and from the optimal simulated case after calibration using PSO algorithm (red). The displacement of the colliding cylinder representing the heart (as defined in Fig. 3) is presented in yellow.

lying on the vessel wall in the radial direction based on *Assumption 1* as shown in Fig. 2. Compared with the reference curve [11], we computed the RMSE (Eq. 5) and minimized it during the automatic PSO calibration process. The optimal cluster parameters were: $[s_c, r_c, t_c]$ =[8 mm, 12 mm, 0.8] with a RMSE of 0.26% while the mean error and standard deviation are 0.23±0.13%. The optimal stress-strain curve is shown in Fig. 7A.

3.1.2. Heartbeat calibration

The objective of heartbeat calibration is to automatically adjust the relevant parameters in the simulator to mimic the annulus displacement in [23]. The reference curve [23] is the averaged annulus displacement from 60 patients with aortic stenosis. It is referred to as the ground truth in calibration. The relevant parameters are the displacement of the virtual heart causing the displacement of the annulus. The PSO approach optimizes these parameters by minimizing the RMSE between the simulated and real aortic annulus displacement. Fig. 7B presents the displacement of the virtual heart, the annulus displacement from literature, and the simulated annulus displacement after calibration, in three cardiac cycles in a time range of $[0, 2.68]$s. The simulated annulus displacement is shown in Fig. 7B with a RMSE (Eq. 8) of 0.90 mm while the mean error and standard deviation are 0.30±0.85mm. The mean absolute error and the standard deviation of the absolute error are 0.64±0.63mm. The median, 90th percentile, and maximum absolute error are 0.31mm, 1.67mm, and 2.44mm, respectively. The simulated annulus displacement has smoother but in-phase positive peaks and sharper anticipated negative peaks. However, the curve frequency was not altered. Therefore, it can mimic the heartbeat movement at a similar frequency, even if the peaks are not the same. The peaks represent the maximum displacement of the annulus plane during cardiac cycles. If the maximum displacement is more of interest, such as the longitudinal displacement of the aortic annulus [41], the objective function of heartbeat calibration can be changed to minimize the error at peaks between the curves.

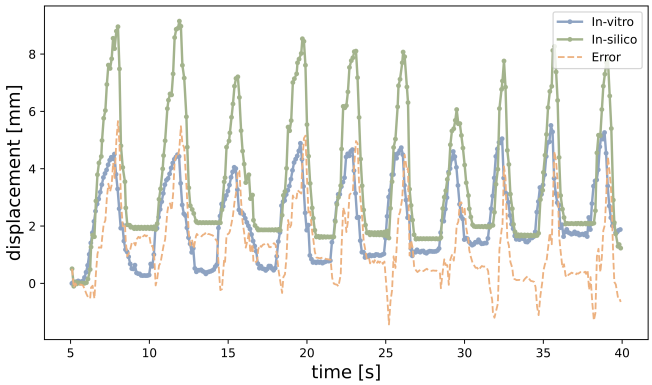

Figure 8: The comparison of displacement obtained during ten different catheter contacts simulated on our PBD model (d_{em}, *in-silico*, green) and the one obtained on the aortic phantom (d_k, *in-vitro*, blue). Their difference is marked in orange. The video comparison is made available: https://youtu.be/2p20Y2-YID8

3.2. In-vitro Validation

We conducted *in-vitro* experiments for the deformed model validation. We compared the displacement obtained during ten different catheter contacts simulated on our PBD model (*in-silico*) and the ones obtained on the aortic phantom (*in-vitro*).

Figure 8 shows the comparison results of vessel deformation obtained in two ways: *in-vitro* and *in-silico*. The mean error and standard deviation are 1.35±1.38mm. The RMSE is 1.93mm. The mean absolute error and the standard deviation of the absolute error are 1.46±1.27mm. The median, 90th percentile, and maximum absolute error are 1.13mm, 3.44mm, and 5.66mm, respectively. The Pearson correlation coefficient between the two curves is 0.83, which indicates a strong positive correlation between the in-silico and in-vitro displacement. It verifies the comparability between the proposed PBD deformed model and the silicone aortic phantom. It also reveals the possibility of further ex-vivo, in-vivo, and patient-specific model validation. One of the error sources can be the inaccurate rigid registration between EM space and simulator space. This inaccuracy results in less accurate correspondence between the second EM sensor and the particle in the PBD model. In this work, a traditional registration method, Singular Value Decomposition (SVD) [42], is performed. More accurate registration methods will help reduce deformation prediction errors.

3.3. End-user Validation

As shown by Table 2, the performance difference between novices and experts shows that novices are more accustomed to using joystick controllers instead of manual operation. Experts spent more time performing task A, i.e., to advance the guidewire from femoral arteries to the abdominal aorta, and task C, i.e., to advance the robotic catheter from the aortic arch to the right coronary ostium. Meanwhile, the experts presented less collision in task C. The comparison results for other tasks do not show statistically significant differences.

The questionnaire results in Fig. 9 show that experts have a higher appraisal of the system, whereas novices are more adapt-

Table 2: Performance comparison of ten novices and ten experts after performing specific operation tasks of PCI, including the operation time of each task and the accumulated collision during the whole task.

Device	**Task**	**User**	**Playtime [s]** (Mean±SD)	**Collision [N]** (Mean±SD)
guidewire	CFA - abdominal aorta	Experts	89.8±38.7 ↕ ⋆	13.2±14.7
	(Fig.6A)	Novices	64.0±25.3	7.3±4.7
	left coronaries angioplasty	Experts	77.8±5.0	3.8±1.7
	(Fig.6D)	Novices	75.6±1.2	3.5±1.7
	right coronaries angioplasty	Experts	71.3±17.0	14.7±11.3
	(Fig.6E)	Novices	68.4±25.5	12.9±6.9
robotic catheter	left coronaries cannulation	Experts	187.8±156.0	5.8±7.8
	(Fig.6B)	Novices	109.1±60.2	2.9±2.6
	right coronaries cannulation	Experts	171.1±111.2 ↕ ⋆	5.0±8.0
	(Fig.6C)	Novices	83.9±46.1	15.2±42.1

⋆, p <0.05 Kruskal-Wallis test for statistical significance analysis

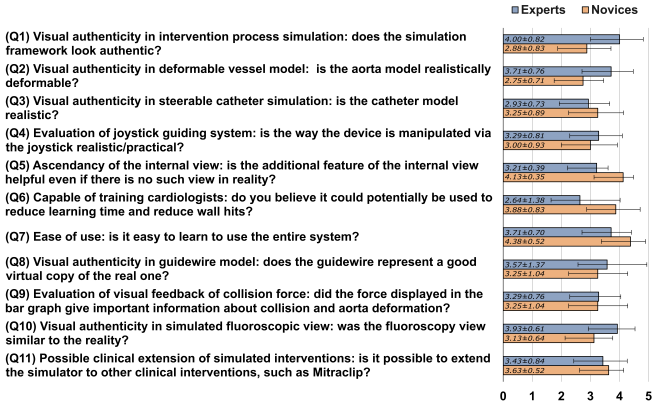

Figure 9: The validity evaluation results of ten novices and ten experts, where Q1-Q11 are the evaluation criteria specified in the questionnaire and 1-5 correspond to the level of agreement: 1-Strongly disagree; 2-Disagree; 3-Neither agree nor disagree; 4-Agree; 5-Strongly agree.

able to novel technologies, such as joystick controllers and simulated internal views. The experts have more diverse opinions on Q6. Two cardiologists rated '1', one cardiologist with three years of experience, and one with six years of experience. The proposed simulator is intended to use as a training platform for robotic catheters [43, 44, 45]. Currently, conventional procedures use flexible catheters without robotic assistance. Cardiologists are more customized to use conventional catheters. Therefore, robot assistance affected the scores on the training capability of the proposed simulator. Scores on other criteria can verify this inference as well. The cardiologists rated higher on Q1 and Q2 and relatively lower on Q3. It shows that the cardiologists are satisfied with the visual authenticity of the intervention process and the deformable property of the vessels. Those are essential factors in a robotic catheter simulation platform.

Constructive feedback on future improvements was provided by cardiologists as well. The coronary guidewire could be modeled with a preshaped nitinol tip with the capability of rotating, which would let it engage different branches of the coronaries. In addition to the heartbeat motion, the respiration motion could be included as well. As for the visual feedback of collision force, haptic feedback such as the vibration of the joystick would be more intuitive. Augmented reality would provide a more visually plausible training.

4. Discussion

4.1. Findings

An important finding of the questionnaire is that cardiologists prefer the internal view of vessels. The internal view of the vessels can be reconstructed from IntraVascular UltraSound (IVUS) images [46]. The internal view is very useful because the cardiologists can only see the structures in 2D in reality without having information about a collision with structures inside vessels. Despite the absence of such a feature in the traditional procedure, it would be helpful to have a real-time 3D view of the anatomy, of the plaques, and devices advancement. What is used in reality is the IVUS view (with a diagnosing catheter) that could be helpful to know about the anatomy and plaques etc., but it is not aligned with the advancement of the balloon/stent catheter because the IVUS view and the intervention treatment are not in the same phase. Despite the absence of such an internal view in the treatment process, the goal is to provide the cardiologists with another perspective that will accelerate the process as they can view the interactions from different views.

4.2. Possibility of Generalization

The deformed model is reconstructed from CTA images of a patient with cardiac disease. It is patient-specific and can be

employed for aorta models of other patients. Heartbeat variability can be achieved as long as a reference curve is given for calibration, such as the reference curve [23].

Even though we used the 6Fr Magellan Robotic Catheter and two specific guidewires as the proof-of-concept, it can be extended to other catheters and guidewires. We can use this simulator to optimize the design of robotic catheters, such as maximum bending extent, steerable tip length, and diameter. Those parameters are adjustable in the proposed simulator. It can also be used for autonomous path planning and control in a simulated, cluttered environment.

4.3. Limitations and Perspectives

The joystick control approach is different from the traditional way to advance devices. Therefore cardiologists expertized in traditional interventions may perform worse than game players. Existing robotic systems mostly use joystick and workstation as the controller input, such as CorPath™ GRX (Corindus), Niobe™ (Stereotaxis) and R-One™ (Robocath). In [47], a device controller is developed that mimics a standard catheter handle, has a vibrotactile feedback, and is easy-to-use by cardiologists. However, joystick controllers with vibrotactile feedback are relatively easy to use and low in cost [14]. We will carry on long-term-following experiments to investigate a proper controller and its training effectiveness.

More operation tasks that reveal expert experience will be carried out in end-user validation. Positioning and inflating a balloon or stent catheter at the occlusion site can be developed as an operation task. This proof-of-concept is presented at the following link: https://youtu.be/lqN4Uw4HZz8. However, accurate simulation of the mechanical properties of the occlusions and stents requires thorough investigation in the future. The accuracy of stent alignment at the target site can be selected as a performance matrix. Moreover, the user's choice of the access route can be assessed to ensure the safety of needle insertion.

Traditional fluoroscopy imaging does not provide enough information for cardiologists, such as depth. Augmented Reality (AR) could be integrated for more visually plausible training [48]. Deformable vessels with AR provide 3D visualization to help guide and locate the instrument more intuitively. Clinical studies in [49] highlight the need for intra-operative 3D visualization to help develop safer interventions. Several commercial systems, such as EnSite NavX (St.Jude), Carto (Biosense Webster), and LocaLisa (Medtronic), develop AR techniques as an alternative to classical imaging techniques.

5. Conclusion

This paper presents a realistic, auto-adaptive, and visually plausible simulator for endovascular catheterization procedures. The proposed workflow implements the modeling and simulation of intervention devices and a deformable aorta that could create a dynamic environment for intra-operative path planning and control in robotic endovascular catheterization, which will be presented in future works. Compared with literature, some novel properties of the proposed simulator are highlighted, such as a simulated movement of the vessels caused by the heartbeat and an autonomous calibration using PSO algorithm. The reported results of *in-vitro* validation show that this simulator framework can be applied to different datasets and represents a good surrogate for the modelization of deformation.

Conflict of Interest

The authors have no conflicts of interest to disclose.

CRediT author statement

Zhen Li: Conceptualization, Methodology, Software, Validation, Writing - Original Draft, Visualization. Enrico Manzionna: Methodology, Software, Writing- Reviewing and Editing, Visualization. Giovanni Monizzi: Writing- Reviewing and Editing, Validation. Angelo Mastrangelo: Writing-Reviewing and Editing, Validation. Maria Elisabetta Mancini: Writing- Reviewing and Editing, Resources. Daniele Andreini: Resources. Jenny Dankelman: Writing- Reviewing and Editing, Supervision. Elena De Momi: Writing- Reviewing and Editing, Supervision.

Acknowledgment

This work was supported by the ATLAS project. This project has received funding from the European Union's Horizon 2020 research and innovation programme under the Marie Sklodowska-Curie grant agreement No 813782. We gratefully acknowledge the support of the Centro Cardiologico Monzino with the resources of the clinical data.

Ethical Approval

The data collection followed the ethical protocol approved by Centro Cardiologico Monzino under the assigned code of *02_21 PA*.

References

[1] F.-J. Neumann, M. Sousa-Uva, A. Ahlsson, F. Alfonso, A. P. Banning, U. Benedetto, R. A. Byrne, J.-P. Collet, V. Falk, S. J. Head, et al., 2018 esc/eacts guidelines on myocardial revascularization, European heart journal 40 (2) (2019) 87–165. doi:10.1093/eurheartj/ehy394.

[2] A. Attanasio, B. Scaglioni, E. De Momi, P. Fiorini, P. Valdastri, Autonomy in surgical robotics, Annual Review of Control, Robotics, and Autonomous Systems 4 (2021) 651–679. doi:10.1146/annurev-control-062420-090543.

[3] G. Koutouzi, M. Pfister, K. Breininger, M. Hellström, H. Roos, M. Falkenberg, Iliac artery deformation during evar, Vascular 27 (5) (2019) 511–517. doi:10.1177/1708538119840565.

[4] B. Maurel, A. Hertault, T. M. Gonzalez, J. Sobocinski, M. L. Roux, J. Delaplace, R. Azzaoui, M. Midulla, S. Haulon, Evaluation of visceral artery displacement by endograft delivery system insertion, Journal of Endovascular Therapy 21 (2) (2014) 339–347. doi:10.1583/13-4471MR.1.

[5] L. Cercenelli, B. Bortolani, G. Tiberi, C. Mascoli, I. Corazza, M. Gargiulo, E. Marcelli, Characterization of vessel deformations during evar: a preliminary retrospective analysis to improve fidelity of endovascular simulators, Journal of Surgical Education 75 (4) (2018) 1096–1105. doi:10.1016/j.jsurg.2017.10.013.

[6] A. Kaladji, A. Dumenil, M. Castro, A. Cardon, J.-P. Becquemin, B. Bou-Saïd, A. Lucas, P. Haigron, Prediction of deformations during endovascular aortic aneurysm repair using finite element simulation, Computerized medical imaging and graphics 37 (2) (2013) 142–149. doi:10.1016/j.compmedimag.2013.03.002.

[7] Z. Li, J. Dankelman, E. De Momi, Path planning for endovascular catheterization under curvature constraints via two-phase searching approach, International Journal of Computer Assisted Radiology and Surgery 16 (4) (2021) 619–627. doi:10.1007/s11548-021-02328-x.

[8] M. Peral-Boiza, T. Gomez-Fernandez, P. Sanchez-Gonzalez, B. Rodriguez-Vila, E. J. Gómez, Á. Gutiérrez, Position based model of a flexible ureterorenoscope in a virtual reality training platform for a minimally invasive surgical robot, IEEE Access 7 (2019) 177414–177426. doi:10.1109/ACCESS.2019.2957857.

[9] A. Hao, J. Cui, S. Li, Q. Zhao, Personalized cardiovascular intervention simulation system, Virtual Reality & Intelligent Hardware 2 (2) (2020) 104–118. doi:10.1016/j.vrih.2020.04.001.

[10] S. Guo, M. Qu, B. Gao, J. Guo, Deformation of the catheter and 3d blood vessel model for a vr-based catheter system, in: IEEE International Conference on Mechatronics and Automation, 2013, pp. 861–866. doi:10.1109/ICMA.2013.6618028.

[11] X. Ye, J. Zhang, P. Li, T. Wang, S. Guo, A fast and stable vascular deformation scheme for interventional surgery training system, Biomedical engineering online 15 (1) (2016) 1–14. doi:10.1186/s12938-016-0148-3.

[12] E. Tagliabue, D. Dall'Alba, E. Magnabosco, C. Tenga, I. Peterlík, P. Fiorini, Position-based modeling of lesion displacement in ultrasound-guided breast biopsy, International journal of computer assisted radiology and surgery 14 (8) (2019) 1329–1339. doi:10.1007/s11548-019-01997-z.

[13] E. Tagliabue, A. Pore, D. Dall'Alba, E. Magnabosco, M. Piccinelli, P. Fiorini, Soft tissue simulation environment to learn manipulation tasks in autonomous robotic surgery, in: 2020 IEEE/RSJ International Conference on Intelligent Robots and Systems (IROS), 2020, pp. 3261–3266. doi:10.1109/IROS45743.2020.9341710.

[14] A. Segato, C. Di Vece, S. Zucchelli, M. Di Marzo, T. Wendler, M. F. Azampour, S. Galvan, R. Secoli, E. De Momi, Position-based dynamics simulator of brain deformations for path planning and intra-operative control in keyhole neurosurgery, IEEE Robotics and Automation Letters 6 (3) (2021) 6061–6067. doi:10.1109/LRA.2021.3090016.

[15] A. Segato, M. Di Marzo, S. Zucchelli, S. Galvan, R. Secoli, E. De Momi, Inverse reinforcement learning intra-operative path planning for steerable needle, IEEE Transactions on Biomedical Engineering 69 (6) (2021) 1995–2005. doi:10.1109/TBME.2021.3133075.

[16] G. Turini, S. Condino, U. Fontana, R. Piazza, J. E. Howard, S. Celi, V. Positano, M. Ferrari, V. Ferrari, Software framework for vr-enabled transcatheter valve implantation in unity, in: International Conference on Augmented Reality, Virtual Reality and Computer Graphics, 2019, pp. 376–384. doi:10.1007/978-3-030-25965-5_28.

[17] H. Sharei, J. Kieft, K. Takashima, N. Hayashida, J. J. van den Dobbelsteen, J. Dankelman, A rigid multibody model to study the translational motion of guidewires based on their mechanical properties, Journal of Computational and Nonlinear Dynamics 14 (10). doi:10.1115/1.4043618.

[18] H. Sharei, T. Alderliesten, J. J. van den Dobbelsteen, J. Dankelman, Navigation of guidewires and catheters in the body during intervention procedures: a review of computer-based models, Journal of Medical Imaging 5 (1) (2018) 010902. doi:10.1117/1.JMI.5.1.010902.

[19] J. Till, V. Aloi, C. Rucker, Real-time dynamics of soft and continuum robots based on cosserat rod models, The International Journal of Robotics Research 38 (6) (2019) 723–746. doi:10.1177/0278364919842269.

[20] C. Della Santina, A. Bicchi, D. Rus, On an improved state parametrization for soft robots with piecewise constant curvature and its use in model based control, IEEE Robotics and Automation Letters 5 (2) (2020) 1001–1008. doi:10.1109/LRA.2020.2967269.

[21] R. J. Roesthuis, S. Misra, Steering of multisegment continuum manipulators using rigid-link modeling and fbg-based shape sensing, IEEE transactions on robotics 32 (2) (2016) 372–382. doi:10.1109/TRO.2016.2527047.

[22] T. da Veiga, J. H. Chandler, P. Lloyd, G. Pittiglio, N. J. Wilkinson, A. K. Hoshiar, R. A. Harris, P. Valdastri, Challenges of continuum robots in clinical context: A review, Progress in Biomedical Engineering 2 (3). doi:10.1088/2516-1091/ab9f41.

[23] H. Nakai, M. Takeuchi, H. Yoshitani, K. Kaku, N. Haruki, Y. Otsuji, Pitfalls of anatomical aortic valve area measurements using two-dimensional transoesophageal echocardiography and the potential of three-dimensional transoesophageal echocardiography, European Journal of Echocardiography 11 (4) (2010) 369–376. doi:10.1093/ejechocard/jep220.

[24] K. Kalisz, J. Buethe, S. S. Saboo, S. Abbara, S. Halliburton, P. Rajiah, Artifacts at cardiac ct: physics and solutions, Radiographics 36 (7) (2016) 2064–2083. doi:10.1148/rg.2016160079.

[25] Z. Liu, Z. Zhang, N. Hong, L. Chen, C. Cao, J. Liu, Y. Sun, Diagnostic performance of free-breathing coronary computed tomography angiography without heart rate control using 16-cm z-coverage ct with motion-correction algorithm, Journal of cardiovascular computed tomography 13 (2) (2019) 113–117. doi:10.1016/j.jcct.2019.01.005.

[26] J. Liang, Y. Sun, Z. Ye, Y. Sun, L. Xu, Z. Zhou, B. Thomsen, J. Li, Z. Sun, Z. Fan, Second-generation motion correction algorithm improves diagnostic accuracy of single-beat coronary ct angiography in patients with increased heart rate, European radiology 29 (8) (2019) 4215–4227. doi:10.1007/s00330-018-5929-6.

[27] B. Mensel, A. Quadrat, T. Schneider, J.-P. Kühn, M. Dörr, H. Völzke, W. Lieb, K. Hegenscheid, R. Lorbeer, Mri-based determination of reference values of thoracic aortic wall thickness in a general population, European radiology 24 (9) (2014) 2038–2044. doi:10.1007/s00330-014-3188-8.

[28] Z. A. Fayad, V. Fuster, J. T. Fallon, T. Jayasundera, S. G. Worthley, G. Helft, J. G. Aguinaldo, J. J. Badimon, S. K. Sharma, Noninvasive in vivo human coronary artery lumen and wall imaging using black-blood magnetic resonance imaging, Circulation 102 (5) (2000) 506–510. doi:10.1161/01.cir.102.5.506.

[29] P. Cignoni, M. Callieri, M. Corsini, M. Dellepiane, F. Ganovelli, G. Ranzuglia, et al., Meshlab: an open-source mesh processing tool., in: Eurographics Italian chapter conference, Vol. 2008, 2008, pp. 129–136. doi:10.2312/LocalChapterEvents/ItalChap/ItalianChapConf2008/129-136.

[30] G. Taubin, Curve and surface smoothing without shrinkage, in: IEEE international conference on computer vision, 1995, pp. 852–857. doi:10.1109/ICCV.1995.466848.

[31] M. Müller, B. Heidelberger, M. Hennix, J. Ratcliff, Position based dynamics, Journal of Visual Communication and Image Representation 18 (2) (2007) 109–118. doi:10.1016/j.jvcir.2007.01.005.

[32] M. Müller, B. Heidelberger, M. Teschner, M. Gross, Meshless deformations based on shape matching, ACM transactions on graphics (TOG) 24 (3) (2005) 471–478. doi:10.1145/1073204.1073216.

[33] M. Jaberipour, E. Khorram, B. Karimi, Particle swarm algorithm for solving systems of nonlinear equations, Computers & Mathematics with Applications 62 (2) (2011) 566–576. doi:10.1016/j.camwa.2011.05.031.

[34] H. Rafii-Tari, C. V. Riga, C. J. Payne, M. S. Hamady, N. J. Cheshire, C. D. Bicknell, G.-Z. Yang, Reducing contact forces in the arch and supra-aortic vessels using the magellan robot, Journal of vascular surgery 64 (5) (2016) 1422–1432. doi:10.1016/j.jvs.2015.06.215.

[35] R. J. Webster III, B. A. Jones, Design and kinematic modeling of constant curvature continuum robots: A review, The International Journal of Robotics Research 29 (13) (2010) 1661–1683. doi:10.1177/0278364910368147.

[36] G. J. Harrison, T. V. How, S. R. Vallabhaneni, J. A. Brennan, R. K. Fisher, J. B. Naik, R. G. McWilliams, Guidewire stiffness: what's in a name?, Journal of Endovascular Therapy 18 (6) (2011) 797–801. doi:10.1583/11-3592.1.

[37] J. Carey, D. Emery, P. McCracken, Buckling test as a new approach to testing flexural rigidities of angiographic catheters, Journal of Biomedical Materials Research Part B: Applied Biomaterials 76 (1) (2006) 211–218. doi:10.1002/jbm.b.30358.

[38] E. Vander Poorten, P. Tran, A. Devreker, C. Gruijthuijsen, S. Portoles-Diez, G. Smoljkic, V. Strbac, N. Famaey, D. Reynaerts, J. Vander Sloten, et al., Cognitive autonomous catheters operating in dynamic environments, Journal of Medical Robotics Research 1 (03) (2016) 1640011. doi:10.1142/S2424905X16400110.

[39] M. Kvasnytsia, N. Famaey, M. Böhm, E. Verhoelst, Patient specific vascular benchtop models for development and validation of medical devices for minimally invasive procedures, Journal of Medical Robotics Research 1 (03) (2016) 1640008. doi:10.1142/S2424905X16400080.

[40] Omnexus, Flexural modulus values of several plastics, https://omnexus.specialchem.com/polymer-properties/properties/stiffness, (visited on 2022-09-13) (2022).

[41] T. Plonek, M. Berezowski, J. Kurcz, P. Podgorski, M. Sąsiadek, B. Rylski, A. Mysiak, M. Jasinski, The evaluation of the aortic annulus displacement during cardiac cycle using magnetic resonance imaging, BMC Cardiovascular Disorders 18 (1) (2018) 1–6. doi:10.1186/s12872-018-0891-4.

[42] K. S. Arun, T. S. Huang, S. D. Blostein, Least-squares fitting of two 3-d point sets, IEEE Transactions on Pattern Analysis and Machine Intelligence PAMI-9 (5) (1987) 698–700. doi:10.1109/TPAMI.1987.4767965.

[43] M. H. D. Ansari, B. Farola Barata, T. Fabian, Z. Li, D. Wu, D. DallÁlba, G. Borghesan, M. Ourak, V. Iacovacci, S. Tognarelli, D. Jenny, E. D. Momi, P. Breedveld, P. Fiorini, J. V. Sloten, A. Menciassi, E. V. Poorten, Proof-of-concept medical robotic platform for endovascular catheterization, in: Proc. of the 11th Conference on New Technologies for Computer and Robot Assisted Surgery (CRAS), 2022, pp. 66–67.
URL https://atlas-itn.eu/wp-content/uploads/2022/05/CRAS2022_ATLAS_C3.pdf

[44] D. Wu, Y. Zhang, M. Ourak, K. Niu, J. Dankelman, E. Vander Poorten, Hysteresis modeling of robotic catheters based on long short-term memory network for improved environment reconstruction, IEEE Robotics and Automation Letters 6 (2) (2021) 2106–2113. doi:10.1109/LRA.2021.3061069.

[45] D. Wu, X. T. Ha, Y. Zhang, M. Ourak, G. Borghesan, K. Niu, F. Trauzettel, J. Dankelman, A. Menciassi, E. Vander Poorten, Deep-learning-based compliant motion control of a pneumatically-driven robotic catheter, IEEE Robotics and Automation Letters 7 (4) (2022) 8853–8860. doi:10.1109/LRA.2022.3186497.

[46] B. F. Barata, P. T. Tran, G. Borghesan, K. McCutcheon, D. Dall'Alba, P. Fiorini, J. Vander Sloten, E. Vander Poorten, Ivus-based local vessel estimation for robotic intravascular navigation, IEEE Robotics and Automation Letters 6 (4) (2021) 8102–8109. doi:10.1109/LRA.2021.3102307.

[47] L. Cercenelli, B. Bortolani, E. Marcelli, Cathrob: A highly compact and versatile remote catheter navigation system, Applied Bionics and Biomechanics 2017. doi:10.1155/2017/2712453.

[48] R. M. Viglialoro, N. Esposito, S. Condino, F. Cutolo, S. Guadagni, M. Gesi, M. Ferrari, V. Ferrari, Augmented reality to improve surgical simulation: Lessons learned towards the design of a hybrid laparoscopic simulator for cholecystectomy, IEEE Transactions on Biomedical Engineering 66 (7) (2018) 2091–2104. doi:10.1109/TBME.2018.2883816.

[49] C. Butter, H. Kaneko, G. Tambor, M. Hara, M. Neuss, F. Hoelschermann, Clinical utility of intraprocedural three-dimensional integrated image guided transcatheter aortic valve implantation using novel automated computed tomography software: A single-center preliminary experience, Catheterization and Cardiovascular Interventions 93 (4) (2019) 722–728. doi:10.1002/ccd.27920.